Self-Referencing TDR Dielectric Spectroscopy Using Reflection-Decoupled Analysis With a Mismatched Section

Yin Jeh Ngui and Chih-Ping Lin

***Abstract*— An innovative self-referencing time-domain reflectometry (TDR) dielectric spectroscopy method is introduced. The method extracts the first reflection from a mismatched section (MS) immediately before the sensing section (SS) to capture the source characteristics and effect of leading sections. A reflection-decoupled analysis (RDA) is derived to characterize the complex dielectric permittivity (CDP) in the ss. Conventional time-domain spectroscopy (TDS) offers a more cost-effective alternative to frequency-domain methods, but its accuracy may suffer from input function variation, system mismatches, and probe design restrictions. RDA with MS approach provides an efficient, robust, and flexible dielectric spectroscopy technique including its calibration, which inherits all advantages of conventional TDS while using more economic TDR device and more flexible probe design. It adopts a nonconductive and nondispersive MS to serve as a reflector for reliable reference source directly embedded in a single TDR signal. Spectral ratios between the reflection from MS and all other reflections from the SS are experimentally determined and matched to the RDA-derived values as a function of CDP. RDA is inherently independent of source function, instrument mismatch, and cable resistance. There are only four frequency-independent system parameters that can be easily calibrated once and for all using a measurement of well-known material. The method is presented in a general framework without major restrictive assumptions, which explicitly expresses all probe parameters, allowing greater flexibility in probe design (e.g., geometric impedance, probe length, and end condition). Robustness of RDA was verified by numerical and experimental investigations using eight materials of different dielectric characteristics.**

***Index Terms*— Complex dielectric permittivity (CDP), dielectric spectroscopy, reflection-decoupled analysis (RDA), time-domain reflectometry (TDR), time-domain spectroscopy (TDS).**

I. Introduction

MATERIAL characterization using dielectric spectroscopy is highly progressive with the emergence of microtechnologies over the past decades. Frequency-dependent material properties are probed by exposing the material-under-test (MUT) under alternating electric field at different frequencies [1]. Phase change and attenuation responses of the induced electromagnetic (EM) field would reflect various dynamic processes of molecules corresponding to different polarization mechanisms in different frequency ranges [2], [3]. Dielectric measurements are usually achieved either using frequency or time-domain techniques, each with their strengths and limitations.

Vector network analyzer (VNA) is among the commonly used dielectric spectroscopy tools to characterize fluids, solids, and composites in frequency domain directly [4]–[6]. However, accurate VNA measurements are laborious, since it requires delicate system calibration and sample preparation in dedicated sample holders. Frequency domain reflectometry (FDR) probes only use a single frequency instead of a frequency range, which simply measured the apparent dielectric constant at the operating frequency. Frequency domain methods generally require multiple measurements at varying sweeping frequencies to fully characterize MUT with a wide spectrum.

Time-domain spectroscopy/time-domain dielectric spectroscopy (TDS/TDDS) method was initially presented by Fellner-Feldegg [7], Nicolson and Ross [8], Claasen and van Gemert [9], and Cole [10] to extract dielectric permittivity from time-domain reflectometry (TDR) signals, covering several megahertz to gigahertz frequency ranges. The major advantage of TDS methods over frequency approaches is their capability of measuring continuous spectrums and acquires values at practically any defined frequency within its bandwidth. The relaxation behavior of MUT may also be captured directly in the time domain, and subsequent relaxation frequency (or time) may be determined through time-frequency conversion [11]. Most TDS approaches involved the comparison of an incident pulse to the reflected pulse measured by a TDR device, in order to characterize complex dielectric permittivity (CDP) spectrum of MUT. As seen early in [7] and [8], they demonstrated the TDS feasibility in CDP measurement through processing scattering coefficient and transmission coefficients from time-domain signals, based on transmission line theory. Multiple reflections of time-domain signals were later incorporated in TDS formulations with thin-sample (cell) method and lumped-element models, which further improved CDP estimation accuracy [9], [12]–[16]. Source function (input from the signal generator) needs to be known for this approach, but this is difficult to be accurately determined and may subject to change with working temperature. Scatter function is derived assuming there is no mismatch and resistive loss in the leading transmission line before the sensing waveguide. This is difficult to achieve in practical less controlled environment. Full waveform approach-based TDS [10], [17]–[21] tackled the CDP inversion using complex

Manuscript received January 1, 2022; revised March 16, 2022; accepted March 30, 2022. Date of publication April 18, 2022; date of current version April 29, 2022. The Associate Editor coordinating the review process was Dr. Daniel Belega. *(Corresponding author: Chih-Ping Lin.)*

The authors are with the Department of Civil Engineering, National Yang Ming Chiao Tung University, Hsinchu 300, Taiwan (e-mail: cplin.ce@nycu.edu.tw).

Digital Object Identifier 10.1109/TIM.2022.3167768

admittance with respect to the complete waveform, taking all reflections into account. TDS using lumped capacitance method was improved using the total difference method [11], [22]–[24] and multiwindow nonuniform sampling [25], pushing the effective measurement frequency up to five orders. This approach treats sample cells as an effective capacitor in formulation but may be limited in approximations at high-frequency range, especially for polar dielectrics [22]. Total reflection methods [13], [22], [26]–[29] perform TDS in terms of reflections $r(t)$ from sample, by comparing extracted $r(t)$ of MUT to some reference reflections with known conditions (e.g., short-open-load (SOL) calibration based on open, short, and known load conditions) using similar transmission line setup. This approach was also known as the bilinear calibration, which may prevent influence due to nonideal conditions within the transmission line. Spectral analysis of CDP using TDS techniques was further used in numerous studies from material science [30], [31], physical chemistry [32]–[34], soil sciences [35]–[41], and other fields. Conventional TDS technique offers a more economical alternative to VNA, but it is sometimes less accurate due to uncertainty in characterization of input function. Besides, most current TDS approaches require specially designed probe or sample holder. Automated acquisition of these individual signals may be particularly difficult in field automation or long-term monitoring.

Emerging demand for rapid yet accurate dielectric spectroscopy tool is imminent for field measurements, such as water quality monitoring, geoenvironmental investigation, and other field of studies. Multiple studies proposed simple yet cost-efficient TDDS approaches, based on single-shot/standalone measurements. Phase velocity analysis (PVA) approach was initially used to perform direct acquisition of apparent dielectric permittivity (ADP) spectrum based on single TDR measurement [42]. Two major reflections of time-domain signal occurring at both ends of sensing probe are extracted using PVA and the corresponding ADP is gathered through their phase shift at various frequencies. PVA is simple, model-free, inversion free TDS approach, but the real and imaginary parts of CDP could not be distinguished in PVA. Hence, dual reflection analysis (DRA) on TDR signals [43] was later proposed to measure CDP spectrum following similar signal processing procedures as PVA, but followed by implicitly solving their spectral ratios using nonlinear optimization for CDP spectrum. Both PVA and DRA perform TDS in a single measurement to obtain ADP and CDP spectrum with satisfactory results in most MUT except for dispersive materials. Dispersive materials would induce signal truncation and leakage, which would narrow the effective frequency range. Lin *et al.* [44] found that by considering the multiple reflections of time-domain signals, multiple reflection analysis (MRA) could further minimize the signal truncation effect at the end of the second (end) reflection from the sensing section (r_2), through the selection of time window at any points after the steady state of time-domain signals for the all remaining reflections, $r_{\text{remaining}}$. MRA is capable of CDP measurement for both dispersive and nondispersive materials at a broader frequency range from 10 MHz to 1 GHz, with extremely simple system calibration for sensing section length only. Slight signal leakage from first (head) reflection (r_1) into $r_{\text{remaining}}$ is still observed for highly dispersive MUT but has certain improvement compared to its predecessors. Window selections for all three methods (PVA, DRA, and MRA) require nominal probe length for the identification and isolation of the first major reflection, which also vary for different MUTs and may potentially influence measured spectrum due to subjective data selection in extreme cases, such as short probes with low CDP MUT. Field implementation would also require the dynamic adjustment on window selection if the CDP fluctuates significantly during monitoring duration.

Inspired by all aforementioned issues, this study proposes a rapid, robust, flexible, and convenient dielectric spectroscopy technique, based on a self-referencing TDR technique, in order to measure the CDP spectrum of material more accurately for a wider frequency range. Instead of using the first reflection from the sensing section as the reference component, a novel stable self-referencing signal is artificially induced by a mismatched section (MS) with well-known dielectric properties. This reflection-decoupled analysis (RDA) is extended from MRA to capture dielectric spectrum of materials robustly through a single TDR measurement. RDA is source function independent and no input scaling is required, as this method compensates for the unknown input using MS signal as the reference waveform. Through incorporating the steady, nonleaking, and nonconductive signal of MS, signal truncation or leakage into the subsequent sensing section can be avoided. Window selection during signal processing is extremely robust compared to PVA, DRA, and MRA. RDA uses a fixed time window at MS for RDA regardless of the MUT at subsequent sensing section, which further enables more flexible probe design. Features of RDA would enable its wide implementation in field dielectric spectroscopy automation.

Theoretical framework of RDA is first validated using numerical assessment, whereas necessary probe design and system calibrations are elaborated subsequently. Implementation feasibility of RDA is also further evaluated using experimental data with multiple MUTs.

II. Methods

A. Reflection-Decoupled Analysis With a Mismatched Section

TDR measurement system normally consists of the following components for typical signal acquisition, which are EM pulse generator, oscilloscope, transmission line, and sensing probe. Measurement setup adapted for RDA is similar to conventional TDR setup, but with an additional MS (also referred to as the probe head) that is introduced purposely. This can be a specially manufactured dielectric block in the probe head or simply a coaxial cable of different characteristic impedances from the leading cable (LC). Detailed probe designs are elaborated later. The nomenclatures used in this study are similar to [44] for consistency. To better illustrate the propagation path of the injected EM wave, measurement setup adapted to the RDA method is shown in Fig. 1.

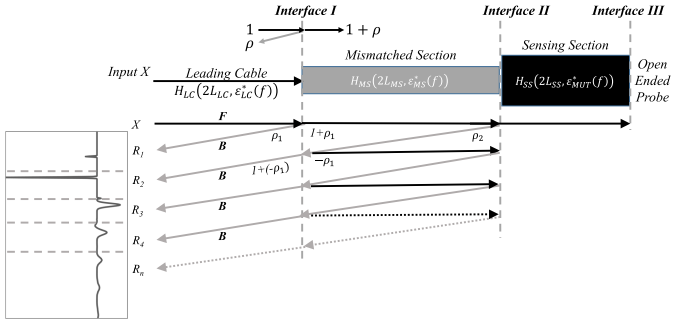

Fig. 1. Ray tracing diagram for RDA.

The fundamental mode of TDR system is the 1-D transverse EM mode [45], and ray tracing approach is used to formulate the wave propagation of TDR signals. Propagation function $H(x, \varepsilon^*(f))$ is used to define the attenuation and phase variation of EM wave during the wave propagation along the transmission line [44]

$$H\big(x, \varepsilon^*(f)\big) = \exp\big[-\gamma(f)x\big] \tag{1}$$

where x is the propagation distance, $\varepsilon^*(f)$ is the CDP, f is the frequency, j is $\sqrt{-1}$, c is the speed of light, and $\gamma(f)$ is the propagation constant, which can be expressed as

$$\gamma(f) = \frac{j2\pi f}{c}\sqrt{\varepsilon^*(f)}. \tag{2}$$

Based on the ray tracing diagram shown in Fig. 1, an input X is injected into the transmission line system and propagated along the LC until Interface I (LC-MS), where part of the forward wave is reflected back to the oscilloscope. The first main reflection pulse r_1 has the spectral representation of R_1

$$R_1 = X \cdot F \cdot \rho_1 \cdot B \tag{3}$$

where F and B are the forward and backward propagating function of the preceding LC, ρ_1 is the reflection coefficient at Interface I, and can be determined from

$$\rho_1 = \frac{Z_{\text{cMS}} - Z_{\text{cLC}}}{Z_{\text{cMS}} + Z_{\text{cLC}}} \tag{4}$$

in which Z_{cLC} and Z_{cMS} are the characteristic impedances of the LC and MS, respectively. Characteristic impedance (Z_c) is a function of geometric impedance (Z_p) and CDP (ε^*). The time-domain and frequency-domain components are expressed using lower case (r_i) and capital case (R_i), respectively.

Remaining signal propagates through the impedance discontinuity at Interface I and into MS. As it arrives at Interface II between probe head (i.e., MS) and sensing section (SS), the impedance discontinuity induces the second major reflection r_2. The corresponding spectral ratio R_2 is

$$\begin{aligned} R_2 &= XF(1+\rho_1)\cdot H\big(2L_{\text{MS}}, \varepsilon^*_{\text{MS}}(f)\big)\cdot \rho_2(1-\rho_1)\cdot B \\ &= XFB\cdot\big[H_{\text{MS}}\big(1-\rho_1^2\big)(\rho_2)\big] \end{aligned} \tag{5}$$

where L_{MS} is the length of the MS, $\varepsilon^*_{\text{MS}}(f)$ is the CDP of the MS, and $H_{\text{MS}} = H(2L_{\text{MS}}, \varepsilon^*_{\text{MS}}(f))$ is the propagation function in the MS. ρ_2 in (5) is the reflection coefficient S_{11} at Interface II, which includes all effects from the sensing section. The derivation of ρ_2 is critical to the RDA and to be explained as follows. In multisection ray tracing, the transmitted signal at Interface II continues to propagate within SS until it reaches Interface III, the open end of the sensing probe. At this interface, total reflection occurs and multiple reflections continue to propagate back and forth as aforementioned, until they ultimately attenuate and reach a steady state. If the ray paths in the SS are traced in this fashion, subsequent multiple reflections are too complicated to be analytically tracked. The concept of input impedance is utilized at Interface II for RDA approach instead of the direct ray tracing method. Lin and Tang [46] used this approach in their comprehensive wave propagation model to recursively lump sum the total impedance response of the entire nonuniform transmission line into a single input impedance (Z_{in}). This is being done in a bottom-up fashion. Following the definition of input impedance, the input impedance at Interface III is:

$$Z_{\text{in(III)}} = Z_L \tag{6}$$

where Z_L is the load impedance and is of infinity value for an open-circuit boundary. The open-ended probe termination is treated as an ideal open; however, certain negligible influence from reactive or possibly radiative effects may occur at Interface III. The end fringing effect is negligible if SS is not ultrashort. It can be further minimized by sharpening the tip of the sensing waveguide. Backing up to Interface II, the input impedance at Interface II is now

$$Z_{\text{in(II)}} = Z_{\text{cSS}}\frac{Z_L + Z_{\text{cSS}}\tanh(\gamma_{\text{SS}}L_{\text{SS}})}{Z_{\text{cSS}} + Z_L\tanh(\gamma_{\text{SS}}L_{\text{SS}})} \tag{7}$$

where L_{SS} and γ_{SS} are the length and frequency-dependent propagation constant of SS, correspondingly, where

$$\gamma_{\text{SS}}(f) = \frac{j2\pi f}{c}\sqrt{\varepsilon^*_{\text{MUT}}(f)}. \tag{8}$$

Since $Z_L = \infty$ for an open-loop boundary, (7) is therefore reduced to

$$Z_{\text{in(II)}} = Z_{\text{cSS}}\left[\frac{Z_L}{Z_{\text{cSS}} + Z_L\tanh(\gamma_{\text{SS}}L_{\text{SS}})}\right]. \tag{9}$$

By L'Hospital rule [47], as Z_L approaches infinity, the input impedance at Interface II becomes

$$Z_{\text{in(II)}} = Z_{\text{cSS}}\cdot\coth(\gamma_{\text{SS}}L_{\text{SS}}). \tag{10}$$

Input impedance method is only used until Interface II as RDA requires the spectral ratio comparison between the first major reflection at Interface I and the rest afterward. Dielectric characteristics of the SS are included in the input impedance at Interface II and ray tracing approach can handle this reduced degree of complexity. The reflection coefficient at Interface II that takes into account of the whole SS can be derived as

$$\rho_2 = \frac{Z_{\text{cSS}}\cdot\coth(\gamma_{\text{SS}}L_{\text{SS}}) - Z_{\text{cMS}}}{Z_{\text{cSS}}\cdot\coth(\gamma_{\text{SS}}L_{\text{SS}}) + Z_{\text{cMS}}}. \tag{11}$$

Further tracing the remaining multiple reflections within the MS after the first two major reflections, they follow the path similar to r_2 but with an additional bounce within the MS.

The spectral content of the resultant $r_3, r_4, \ldots, r_n$ can be expressed as

$$R_3 = X \cdot F \cdot B \cdot \left[H_{\mathrm{MS}}\left(1-\rho_1^2\right)(\rho_2)\right] \cdot [-\rho_1\rho_2 H_{\mathrm{MS}}] \quad (12)$$

$$R_4 = X \cdot F \cdot B \cdot \left[H_{\mathrm{MS}}\left(1-\rho_1^2\right)(\rho_2)\right] \cdot [-\rho_1\rho_2 H_{\mathrm{MS}}]^2. \quad (13)$$

Extending these multiple reflections up to r_n, the spectral representation from r_2 to r_n is generalized into

$$R_k = X \cdot F \cdot B \cdot \left[H_{\mathrm{MS}}\left(1-\rho_1^2\right)(\rho_2)\right] \cdot [-\rho_1\rho_2 H_{\mathrm{MS}}]^{(k-2)} \quad (14)$$

for $k = 2, 3, \ldots, n$.

As proposed by Lin and Tang [46], cable resistance effect can be considered in the formulation by including a resistive correction factor term A in Z_c and γ at any specific sections. A is a function of combined cable resistance effect from geometric factors and surface resistivity due to skin effect, which can be expressed as

$$A = \sqrt{1 + (1-j)\frac{\alpha_R}{\sqrt{f}}} \quad (15)$$

where α_R is the resistive loss factor (unit $\mathrm{s}^{-0.5}$). Any simulated section may include the cable resistance effect through the formulation in their Z_c and γ in the following:

$$Z_c = \frac{Z_p}{\sqrt{\varepsilon^*}} \cdot A \quad (16)$$

$$\gamma = \frac{j2\pi f}{c}\sqrt{\varepsilon^*} \cdot A \quad (17)$$

where Z_p is the geometric impedance (i.e., the characteristic impedance in air).

Similar to MRA [44], RDA measures the MUT's CDP spectrum by comparing the spectral ratio of extracted signals, which cancels out all preceding system functions X, F, and B. The resultant reflection decoupled ratio (RDR) is therefore a function of Z_{cLC} and the system parameters in the MS and SS sections. RDA compares the spectral ratios of the subsequent reflections after r_1 (hereinafter referred to as $r_{\mathrm{remaining}}$) to r_1.

$R_{\mathrm{remanining}}$ is the spectral representation of $R_2+R_3+\cdots+R_n$, which can be determined from the summation of (14)

$$\sum_{k=2}^{\infty} R_k = XFB\left[H_{\mathrm{MS}}\left(1-\rho_1^2\right)(\rho_2)\right] \cdot \sum_{k=2}^{\infty}[-\rho_1\rho_2 H_{\mathrm{MS}}]^{(k-2)}. \quad (18)$$

Applying geometric series summation to the last summation term by substituting $k = n + 2$

$$\sum_{n=0}^{\infty}[-\rho_1\rho_2 H_{\mathrm{MS}}]^n = \frac{1}{1-(-\rho_1\rho_2 H_{\mathrm{MS}})} \quad (19)$$

where $|-\rho_1\rho_2 H_{\mathrm{MS}}| < 1$ must be satisfied for this summation to be valid, whereas $\rho_1 \neq 0$ and $\rho_2 \neq 0$ for nontrivial scenarios. Substituting (19) into (18), $R_{\mathrm{remaining}}$ is thus

$$R_{\mathrm{remaining}} = XFB\left[H_{\mathrm{MS}}\left(1-\rho_1^2\right)(\rho_2)\right] \cdot \frac{1}{1+\rho_1\rho_2 H_{\mathrm{MS}}}. \quad (20)$$

Recalling the definition of RDA, (20) is compared to (3) to obtain its RDR

$$\mathrm{RDR} = \frac{R_{\mathrm{remaining}}}{R_1} = \frac{\rho_2 H_{\mathrm{MS}}\left(1-\rho_1^2\right)}{\rho_1(1+\rho_1\rho_2 H_{\mathrm{MS}})}. \quad (21)$$

The cancellation of XFB in (21) indicates that RDA is source function independent, whereas CDP is measured through a single-shot measurement. Minor mismatches and cable resistance may exist in the path of forward and backward (propagation path) (FB) including the source mismatch. Reflections due to these mismatches and resistance effect can also be absorbed in (21) through the spectral ratio. There are six system parameters involved in (21), including Z_{cLC}, Z_{pMS}, $\varepsilon^*_{\mathrm{MS}}$, L_{MS}, Z_{pSS}, and L_{SS}, only four of which are independent when their combined effect on RDR is considered [e.g., ρ_2 depends on $Z_{\mathrm{pSS}}/Z_{\mathrm{pMS}}$ in (11)]. Calibration of system parameters will be discussed in Section IV. It is noted here that the entire frequency range of a single-shot measurement is used to calibrate four system parameters in RDA, while SOL calibration in VNA or conventional TDS is performed for each single frequency (i.e., three equations and three unknowns for each frequency) without data redundancy to mitigate measurement errors. Furthermore, although SOL calibration can implicitly characterize the incident pulse, recalibration prior to measurements is necessary when characteristics of TDR instrument change over time, for example, due to temperature variation. The major advantages of RDA are its immunity to the variation (albeit transient jitter or device replacement) of TDR instrument and its single-shot calibration without the need for recalibration. The performance of RDA is further evaluated in the numerical appraisal section and is compared against previous approaches in [43] and [44].

B. Signal Processing and Nonlinear Optimization

Following the theoretical framework derived for spectral RDR, detailed analysis procedures using RDA technique to perform complex dielectric spectroscopy are introduced in this section. In order to compute the spectral ratios from the time-domain TDR signals, certain signal preprocessing is required to extract the necessary data. CDP is estimated by fitting the theoretical RDR ($\mathrm{RDR}_{\mathrm{theo}}$) to the measured RDR ($\mathrm{RDR}_{\mathrm{mea}}$) at each frequency, through a model-free nonlinear optimization algorithm. Dielectric model-based inversion may also be attempted instead of model-free inversion, but the inversion soundness may rely on the selected dielectric model. This may be unsuitable for composite materials with unclear governing model. As observed in (21), $\mathrm{RDR}_{\mathrm{theo}}$ is a function of ρ_1, ρ_2, and H_{MS}, where all three system parameters are ultimately linked to the MUT's CDP. Therefore, the optimum CDP (the real and imaginary parts of CDP that fit the resultant $\mathrm{RDR}_{\mathrm{mea}}$) is searched using the Nelder–Mead simplex direct search optimization algorithm [48].

$\mathrm{RDR}_{\mathrm{mea}}$ is acquired through some signal extractions from the measured waveform. Similar to MRA, the recorded time-domain signals must allow the steady state to fully develop and fully include the multiple reflections. The recording time may vary for different lengths of MS and SS. However, the required recording time can be determined by immersing SS into MUT with large CDP (for example, tap water), in order to confirm the largest recording time for any particular RDA measurement setup. This study simulated approximately 2×10^{-7} s recording time unless stated otherwise.

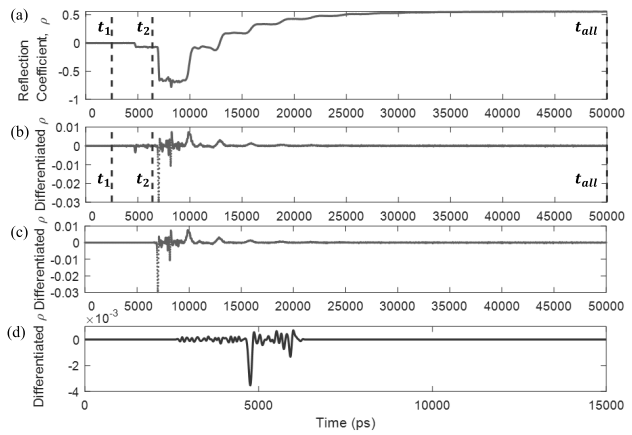

Fig. 2. RDA signal extraction (tap water as example). (a) TDR step signal. (b) Differentiated signal. (c) Extracted $\mathbf{r_{remaining}}$. (d) Extracted $\mathbf{r_1}$.

Fig. 2(a) shows a simulated step pulse TDR signal of tap water with RDA measurement setup, where an MS is placed prior to the SS. The simulated MS has a characteristic impedance lower than that of the LC; hence, the step pulse drops at the MS. In order to facilitate the implementation of fast Fourier Transform (FFT) [49], the step pulse signal is differentiated into pulse signal, as shown in Fig. 2(b). This is to ensure that the truncated signals have close to zero values at the front and end points.

r_1 is extracted from the point t_1 to t_2, in which the former point can be anywhere within the 50-Ω LC. The latter point is suggested to be near the interface between MS and SS, as long as the r_1 signal has reached a steady state and free from the input aberration. This implied that there is a minimum propagation time for the MS, in order to prevent signal leakage or truncation in case r_1 has not reached steady state in due course of wave propagation. $r_{\text{remaining}}$ is truncated from t_2 onward until the end of acquired signal at t_{all}, as shown in Fig. 2(b). It is important to note that the RDA is significantly robust in terms of window selection, compared to PVA [42], DRA [43], and MRA [44]. The window selection for t_1 and t_2 is fixed upon system calibration regardless of the MUT in SS for future measurements, since the MS stays constant throughout the measurements.

Tukey window [50] and low-pass filter are applied for all extracted signals to minimize impact from random noise. Tukey window is applied near the tranquil state at two ends of the truncated signal to avoid the signal edge effect from random noise. Extracted signals are zero-padded to increase the frequency resolution (df). Low-pass filter at 1.5 GHz is finally applied to the extracted signals. Processed signals of $r_{\text{remaining}}$ and r_1 are shown in subplots Fig. 2(c) and (d), respectively.

Upon extracting necessary signals in Fig. 2, their frequency domain is transformed using FFT. RDR_{mea} is obtained by comparing $R_{\text{remaining}}$ to R_1. CDP measurement is conducted by fitting RDR_{theo} with the estimated CDP to match RDR_{mea} at the minimum residual error. This is performed frequency-by-frequency from 1 MHz to 1 GHz (typical TDR effective frequency range) using the *fminsearch* function in

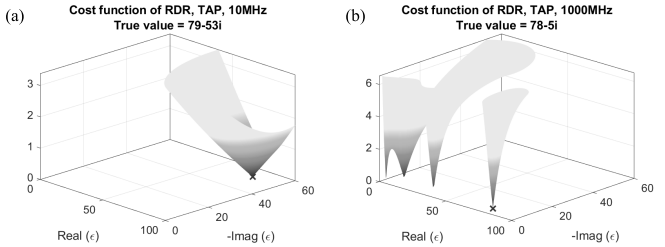

Fig. 3. Cost function structure of theoretical RDR for tap water. (a) RDA at 10 MHz. (b) RDA at 1 GHz.

MATLAB [51], which is a nonlinear optimization algorithm based on Nelder–Mead simplex direct search algorithm.

Nonlinear optimization algorithm, unlike the global optimization techniques, may suffer from local minima. For certain cost function structures, local minimums may exist while true nonuniqueness may occasionally exist at higher frequencies (usually above 500 MHz). Different supplied initial guesses may lead to erratic outcomes. This is due to the nature of nonglobal optimization algorithms, which reduces the cost along a single optimization path, and may stuck within nearby local minimums in case the initial guess is significantly deviated away from true value. To address the issue of local minimum or nonuniqueness, this study proceeded with nonlinear *fminsearch* algorithm but using an iterated initial guess approach. The inversion starts at the lowest frequency, and the estimated CDP is used as the initial value for the next frequency. This was first proposed in MRA [44], where the authors realized that the cost function structure is typically well behaved in lower frequencies without the problem of local minimum or nonuniqueness.

The cost function structures were examined to confirm the feasibility of the iterated initial guess approach for RDA. Cost function structure of RDR_{theo} is plotted for tap water with RDA measurement setup of $L_{\text{MS}} = 0.15$ m, $Z_{\text{cMS}} = 43\ \Omega$, $L_{\text{SS}} = 0.05$, and $Z_{\text{pSS}} = 97\ \Omega$. Cost function structures with different CDP combinations are plotted in Fig. 3 at 10 MHz and 1 GHz. The true CDP value is plotted as "x" at the global minimum. Fig. 3(a) demonstrates that the cost function structure at lower frequency is well-posed. However, as the frequency increases, nonuniqueness issue and local minimums in cost function would arise. The cost structure shown in Fig. 3(b) has multiple local minimums quite close to the global minimum. This creates a relatively ill-posed condition and may lead to incorrect solutions, particularly when a highly deviated initial guess is supplied. This phenomenon of increasing local minimums at high frequency is evaluated and verified identical for different MUTs and various RDA measurement setups.

Based on this unique observation, this study adopted the iterated initial guess method similar to MRA method. Since the cost function structure is well-structured at lower frequencies, CDP optimization initiates from the lowest frequency with an arbitrary CDP $\varepsilon^*_{\text{MUT,ini},f(i)}$ supplied as the initial guess. Due to the well-posed cost function structure at the lowest frequency, a correctly inverted $\varepsilon^*_{\text{MUT,out},f(i)}$ is generated from the *fminsearch* algorithm. This output is next supplied as the initial guess for the next frequency step, $\varepsilon^*_{\text{MUT,ini},f(i+1)}$ and

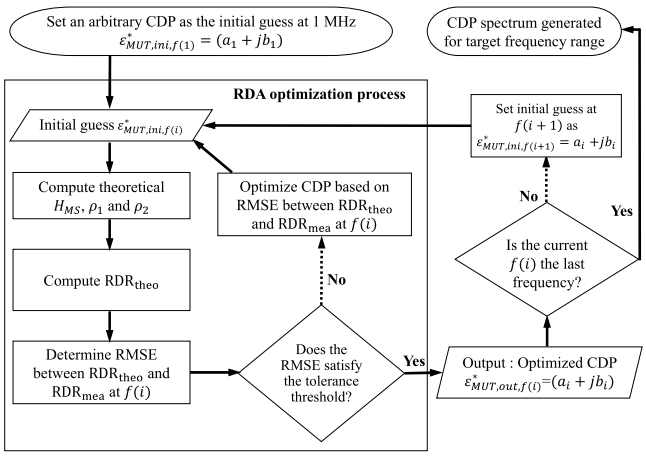

Fig. 4. Flowchart of iterated initial guess implementation in RDA.

the CDP optimization carries on identically until the end of frequency range, as demonstrated in the flowchart of Fig. 4. An arbitrary yet reasonable initial guess of $10 + i$ was used at the lowest frequency for every measurement in this study.

Given an appropriate initial guess, theoretical system functions H_{MS}, ρ_1, and ρ_2 can be calculated by substituting the supplied initial guess into (21). Calibration of some system parameters in the three system functions is required in experimental data. The resultant $\mathrm{RDR_{theo}}$ is compared to the $\mathrm{RDR_{mea}}$ in order to obtain their residual error. The root-mean-square error (RMSE) is used as the cost function to be minimized for the optimized CDP. This minimization process is repeated for every frequency step until the full CDP spectrum is measured.

With the signal processing and CDP optimization procedure for RDA measurement in place, the proposed RDA approach is assessed using synthetic TDR signals and compared against previous methods for performance evaluation.

III. Numerical Assessment

A. Forward Modeling of TDR Signals

The theoretical validity of RDA was first appraised numerically using synthetic TDR signals simulated through a comprehensive wave propagation model established in [46]. Their simulation model allowed individual definition for section length, geometric impedance, CDP spectrum, and resistive loss factor at each section. Cole–Cole model [2] was opted to describe the dielectric spectrum for each simulated section. This study simulated a simple three section transmission line model to evaluate the performance of RDA, consisting of an LC, a probe head (MS), and a coaxial SS. The leading section was selected as 10 m with $Z_{\mathrm{cLC}} = 50\ \Omega$ to accommodate for the LC length used in future field measurement. LC's CDP was assumed as $1 + 0i$ at all frequencies as cables tend to have insignificant relaxation behavior. The resistance loss factor (α_R) was assumed as 50 $\mathrm{s}^{-0.5}$ for the LC, to mimic a mild cable resistance effect. MS was set as 400 mm with $Z_{\mathrm{pMS}} = 150\ \Omega$ and $\varepsilon^*_{\mathrm{MS}} = 5$, in order for the r_1 signal to reach the steady state. SS was set as 170 mm with Z_{pSS} of 97 Ω. These dimensions were such so that a performance comparison can be made between this study and [43], [44] on a similar basis. Recording time was 1.3107×10^{-6} s for each signal based on the MUT with the largest CDP in the current measurement setup.

The input function used in the numerical simulation was measured at 5-ps sampling time by applying a 50-Ω RF terminator on a TDR3000 device (Sympuls Aachen, Germany), resulting in 97-ps rise time. Simulation using an ideal step pulse (e.g., error function) as the input function in [46] would result in perfect fitting to theoretical CDP spectrum, since there is no influence from random noise or signal aberration. Numerical simulation using ideal inputs is favorable to theory validation, but this would be ignorant in facing potential issues lurking in actual applications. Therefore, supplying the recorded TDR3000 signal as the input function in numerical simulation would assist us to understand potential setbacks and their corresponding countermeasures.

Eight MUTs with distinct dielectric dispersion and electrical conductivity properties were simulated. The selected nondispersive MUTs were distilled water, tap water, acetone, and air, whereas the dispersive MUTs were alcohols, including methanol (MTH), ethanol (ETH), isopropanol (IPA), and butanol (BUT). Their Cole–Cole parameters and abbreviations are listed in Table I.

TABLE I
Cole–Cole Parameters of Simulated MUTs

MUT	Abbrev.	ε_{dc}	ε_∞	f_{rel} (GHz)	β	σ_{dc} ($\mu S/cm$)
Distilled water [36]	DIS	80.20	4.22	17.40	0.0125	0
Tap water [36]	TAP	78.54	4.22	17.00	0.0125	300
Acetone [53]	ACE	21.20	1.90	47.65	0	0
Air [44]	AIR	1.00	1.00	-	0	0
Methanol [53]	MTH	33.64	5.70	3.002	0	0
Ethanol [54]	ETH	25.50	4.25	0.782	0	0
Isopropanol [55]	IPA	19.34	2.48	0.448	0	0
Butanol [56]	BUT	17.70	3.30	0.274	0	0

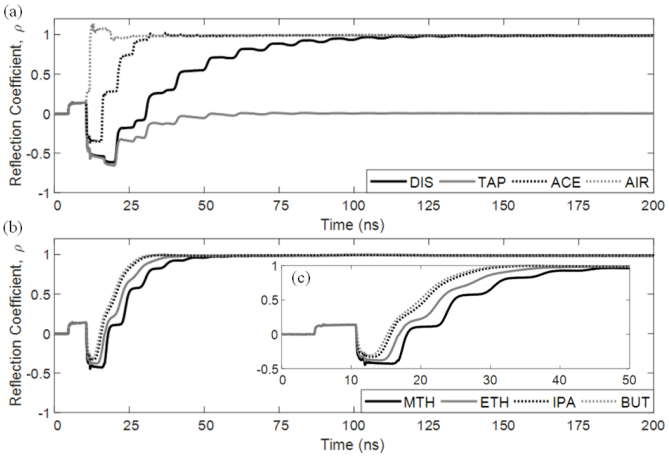

Fig. 5. Simulated TDR signals. (a) Nondispersive MUT. (b) Dispersive MUT. (c) Zoomed-in signals of (b).

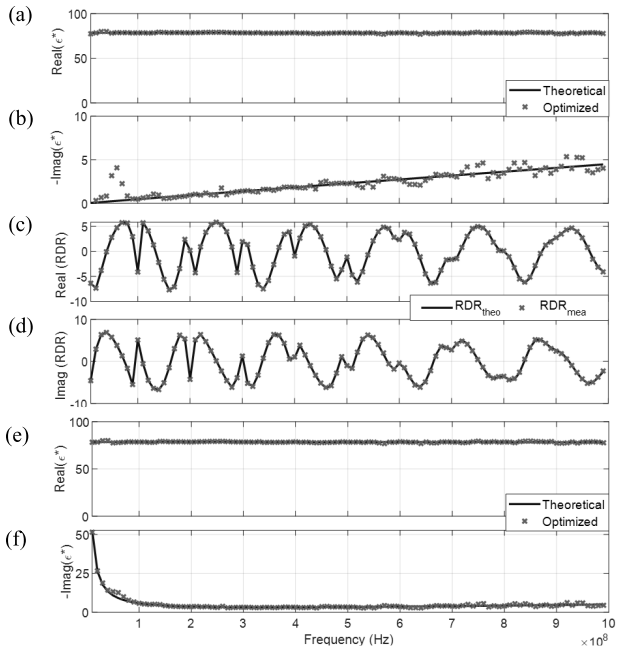

Fig. 6. RDA on simulated signals. Distilled water: (a) real CDP and (b) imaginary CDP and (c) real and (d) imaginary parts of RDR. Tap water: (e) real CDP and (f) imaginary CDP.

The simulated TDR signals shown in Fig. 5 are truncated at 1 m before the MS for a window length of 2×10^{-7} s. This is found sufficient for the multiple reflections to reach the steady state in this particular measurement setup. Nondispersive and dispersive MUTs are plotted separately in Fig. 5(a) and (b). Dispersive MUTs have relatively close CDP value, so close-up view at the MS and SS sections is shown in Fig. 5(c) for inspection. Regarding the selection of signal window for current setup, t_2 is selected at 9.5 ns from the start of signal recording before the waveform plunge at the MS–SS interface, whereas t_1 and t_{all} can be selected arbitrarily at the front (1 ns) and end (200 ns) of the signal.

B. Implementation on Simulated Signals

All signals were processed using the outlined RDA procedures. CDP spectrum was computed from 1 MHz to 1 GHz at 5-MHz frequency interval. Certain system parameters were supplied identical to forward modeled values in numerical simulation, which, however, were undetermined for experimental data. Their calibrations will be discussed in Section III-C prior to the presentation of experimental outcomes.

Measured CDP spectrums for all MUT are plotted in Figs. 6–9, with subfigures illustrating the measured real and imaginary parts of CDP. Theoretical CDP curve and RDR_{mea} used in forward modeling are plotted as solid lines for comparison. Inspecting Fig. 6(c) and (d), RDR_{mea} (marked as "x") matches the theoretical values quite well, thus validating the proposed RDA approach. RDR spectrums are only plotted for DIS because similar well-fitted condition is observed in other MUTs, so theirs are omitted for conciseness.

Deducing from the overall CDP inversion, the implementation of iterated initial guess in RDA is proven to be an effective approach, in order to tackle increasing local minimums in the cost function structures at higher frequencies. Slight scattering at certain frequencies is observed for certain MUT, and this is mainly due to the random noise recorded in the input function, which propagated into the simulated signal, and lower sensitivities in these frequencies. The measurement performance of numerical simulations is further summarized in Table II using statistical analysis on the absolute error of measured CDP within 1 MHz–1 GHz. The mean absolute error across our target frequencies ranged from 0.01 to 0.9 and $0.01i$ to $0.8i$ for real and imaginary parts of CDP, respectively. The standard deviations (STDs) are lower than 1.5 for both real and imaginary parts of CDP, which suggest a closely clustered data around the mean absolute error.

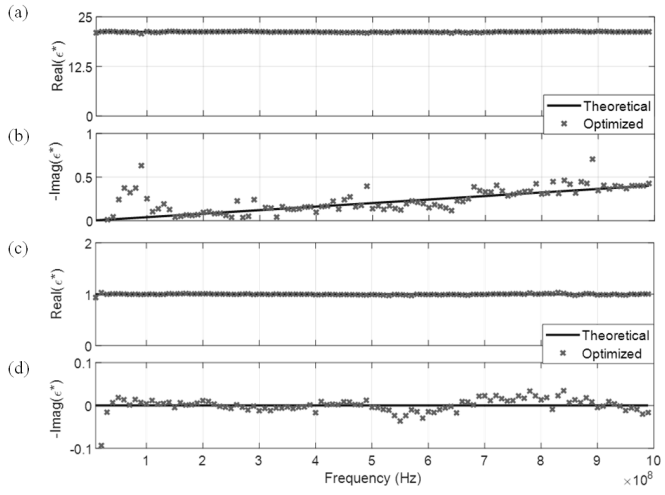

Fig. 7. RDA on simulated signals. (a) Real and (b) imaginary CDP of acetone. (c) Real and (d) imaginary CDP of air.

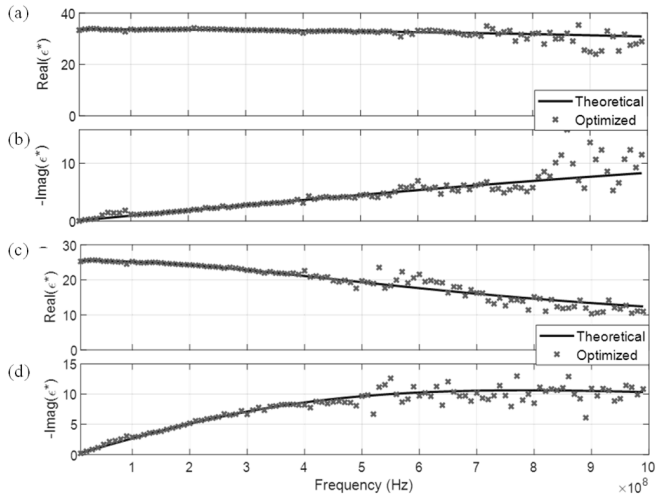

Fig. 8. RDA on simulated signals. (a) Real and (b) imaginary CDP of MTH. (c) Real and (d) imaginary CDP of ETH.

C. Appraisal of DRA, MRA, and RDA

Reliability and performance of RDA were demonstrated with numerical simulation using MUTs of diverse dielectric

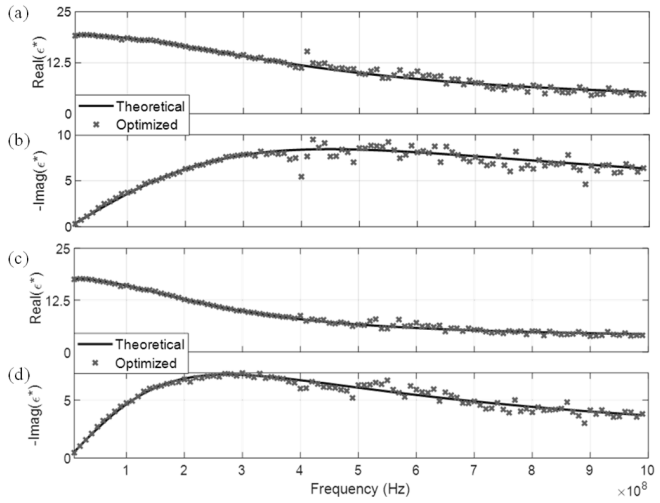

Fig. 9. RDA on simulated signals. (a) Real and (b) imaginary CDP of IPA. (c) Real and (d) imaginary CDP of BUT.

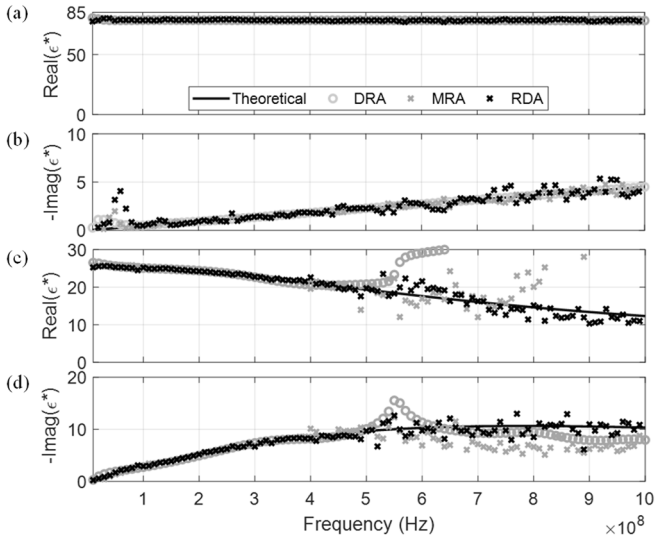

Fig. 10. CDP spectrum measured by DRA, MRA, and RDA. (a) and (b) Real and imaginary CDP of DIS. (c) and (d) Real and imaginary CDP of ETH.

TABLE II

ABSOLUTE ERRORS OF NUMERICAL DATA BETWEEN 1 MHz AND 1 GHz

MUT	Real CDP		Imaginary CDP	
	Mean	STD	Mean	STD
Distilled water	0.35	0.34	0.38	0.55
Tap water	0.40	0.36	0.45	0.56
Acetone	0.08	0.07	0.07	0.09
Air	0.01	0.01	0.01	0.02
Methanol	0.90	1.52	0.81	1.35
Ethanol	0.90	1.08	0.68	0.79
Isopropanol	0.49	0.54	0.40	0.46
Butanol	0.30	0.32	0.26	0.22

TABLE III

ABSOLUTE ERROR COMPARISON AMONG DRA, MRA, AND RDA BETWEEN 10 MHz AND 1 GHz

MUT	Approach	Real CDP		Imaginary CDP	
		Mean	STD	Mean	STD
Distilled water	DRA	0.04	0.19	0.05	0.16
	MRA	0.20	0.22	0.18	0.24
	RDA	0.35	0.33	0.38	0.55
Ethanol	DRA	9.81	10.11	1.20	1.18
	MRA	5.65	9.99	1.71	1.79
	RDA	0.90	1.08	0.68	0.79

characteristics. Prior to this method, DRA and MRA were proposed to retrieve complex dielectric spectrum from TDR signals. To compare their degree of improvements, performance appraisal on all three approaches was conducted numerically with measurement setup similar to Section III-B, where no probe head was simulated for DRA and MRA. CDP spectrums for all three methods were computed from 10 MHz to 1 GHz at 5-MHz frequency interval for equal comparison, as DRA and MRA may only have effective frequency down to 10 MHz.

Two MUTs were selected for approach comparison, DIS as the nondispersive MUT and ETH as the dispersive MUT. The measured CDP spectrums for both MUT are shown in Fig. 10, with outcomes stacked together for direct inspection. Quantitative analysis for the average and STD of absolute errors for all three approaches is also tabulated in Table III. For DIS, all methods have similar performance across all frequencies, whereas their lower frequencies are influenced by the cable resistance effect. Their absolute errors do not differ significantly as seen in both real and imaginary parts of CDP, and all mean absolute error values are below 0.4. CDP spectrum scattering for MRA and RDA is slightly higher than DRA, mostly due to the inclusion of noise in the multiple reflections (DRA only takes the first two major reflections). Absolute errors of MRA and RDA also increase slightly compared to DRA, as seen in Table III.

Nonetheless, the benefit from the inclusion of multiple reflections is observed in the dispersive media. The effective bandwidths of MRA and RDA are higher than DRA in ETH, as the inclusion of multiple reflections has completely captured signal dispersion while reducing the signal truncation effect. Table III shows that DRA has the highest mean absolute error of $9.81 + 1.20i$ and MRA has an intermediate $5.65 + 1.71i$, while RDA has the lowest mean absolute error of $0.9 + 0.68i$. The CDP spectrum of RDA also has the least scattering and deviation from theoretical values.

Among the three methods, RDA performs the best overall, especially in terms of effective bandwidth for both materials. Despite the broader measured CDP spectrum, simpler pulse selection window and no need for long probes are among the powerful features of RDA. This would enable robust measurement and monitoring of dielectric spectroscopy to be performed, regardless of laboratorial or field environment.

Unlike PVA [42], DRA [43], and MRA [44], the impact of signal leakage from r_1 into $r_{\text{remaining}}$ is not observed anymore in RDA, even for very dispersive alcohols with high dielectric loss. This is all attributable to the well-controlled, nonconductive, nonleaking r_1 signal from the MS. However, with the presence of significant cable resistive loss, the time required for r_1 to reach steady state may be prolonged. Mild cable resistance effect ($\alpha_R = 50\ \text{s}^{-0.5}$) was included in the

simulation, where only a slight deviation in the measured spectrum is observed at lower frequency region for RDA, especially for the dispersive ETH. This influence is considerably reduced compared to MRA [44] due to less signal leakage from MS. When a long LC must be used in the field, countermeasure to the cable resistance effect is an ongoing effort to further improve low-frequency measurement and to expand the effective bandwidth.

D. Probe Design

Certain probe design is required to ensure the signal integrity and measurement sensitivity of RDA method. Section III-C reveals that the signal integrity of r_1 (MS) is the most critical factor in RDA to achieve accurate measurements with broader effective bandwidth. Imperatively, the material selection for MS must strictly adhere to nonconductive, nonresistive, and nondispersive dielectric properties for high signal integrity. This is to ensure that r_1 has reached the steady state as soon as possible within the supplied MS length, so that no signal leakage is introduced into subsequent sections. MS does not have to be very long in practice, provided that the combination of the length and material CDP of MS allows r_1 to fully develop and saturates to its steady state, prior to the MS–SS interface. MS material with higher ε^* can prolong the travel time of EM wave in MS, thus permitting the usage of shorter length in MS. On the other hand, the length of SS (L_{SS}) can be of arbitrary length, as the window selection only requires t_2 to be made within r_1, regardless of L_{SS}.

This study also found that both ρ_1 and ρ_2 should be enhanced to allow much of the transmitted signal to be reflected at both LC-MS and MS-SS interfaces, to have sufficient signal-to-noise ratio. The clear characteristic impedance (Z_c) contrast at these interfaces can be designed by adjusting the CDP of MS and Z_p of both MS and SS. If the eventual Z_c values of LC, MS, and SS are similar, the measurement condition would not satisfy the RDA requirement and would be reduced to LC-SS measurement setup.

Feasibility and potential performance of any probe design can be assessed using sensitivity analysis, which is determined by taking the partial derivative of RDR magnitude with respect to the real and imaginary parts of CDP. Sensitivity of RDA to the real and imaginary parts of CDP is denoted as S_1 and S_2. Sensitivity distributions of any specific measurement setup may be simulated for MUT with known CDP spectrum, which could provide insights on potential frequency range with low sensitivity. Even though sensitivity analysis is evaluated analytically and may not consider possible effects from noise, signal truncation, and leakage, this approach would still provide insights and predictions as to how well any specific measurement setup would perform. Further verification on probe design could be carried out numerically through the aforementioned forward modeling with noise inclusion.

IV. System Parameter Calibration

Accurate CDP inversion requires precise system parameter calibration. This calibration is required to be performed only once after the designated RDA probe is connected to the transmission line system. No recalibration is needed even if the broadband TDR pulser is different since the influence from source function variation is canceled out through the formulation.

Deducing from (21), six system parameters are involved, namely, $Z_{\mathrm{cLC}}, Z_{\mathrm{pMS}}, \varepsilon^*_{\mathrm{MS}}, L_{\mathrm{MS}}, Z_{\mathrm{pSS}}$, and L_{SS}. Fewer undetermined system parameters could reduce the complexity of the optimization problem. Careful examination of the RDA functions reveals that there are only four independent variables in the system, which are $L_{\mathrm{MS}}, \varepsilon^*_{\mathrm{MS}}, L_{\mathrm{SS}}$, and Z_{pSS}) or $L_{\mathrm{MS}}, Z_{\mathrm{pMS}}, L_{\mathrm{SS}}$, and Z_{pSS}. The other two parameters may be arbitrarily chosen, and these four parameters can be calibrated to fit the measurement. In order to have a repeatable calibration and to form a less complex global optimization problem, four-parameter calibration was adopted.

System calibration involving all these undetermined parameters would require global optimization algorithm to solve conjunctively for their appropriate values. This study adopted the global optimization algorithm *GlobalSearch* in MATLAB [51]. The *GlobalSearch* algorithm was proposed by Ugray *et al.* [52], where *fmincon* function is applied at multiple trial points and several optimization stages involving basin initialization, counter register for basin, and basin threshold determination. *fmincon* with *sqp* type algorithm was selected for this task as this algorithm can recover from NaN or Inf results and allows optimization boundaries to be allocated and satisfied at all iterations. *GlobalSearch* implements *fmincon* function iteratively with different optimization stages and uses conditional expressions, in order to determine whether the global minimum is found after comparing results at all trial points. This study has attempted other global optimization algorithms, such as simulated annealing, genetic algorithm, and so forth, which eventually found *GlobalSearch* algorithm highly capable of providing consistent and reproducible calibration results. The calibration frequency range for global optimization is dependent on the signal-to-noise ratio, where only the identified effective frequencies are allocated in the calibration. Otherwise, spectral distortion from noisy signal would result in erratic calibration outcome. Effective bandwidth may be identified by stacking $\mathrm{RDR}_{\mathrm{mea}}$ spectrums from multiple measurements.

RDA calibration starts by measuring any material with known CDP spectrum and providing the corresponding $\varepsilon^*_{\mathrm{MUT}}$ as the fitting basis of calibrated RDR ($\mathrm{RDR}_{\mathrm{calib}}$) in the global optimization. During initial trial of system parameter calibration, this study discovered that certain calibration materials could provide satisfactory outcome, while some others may fail even if their true value is supplied as the initial guess. A good calibration material should have an evenly distributed sensitivity without much low sensitivity region or drastic value differences (such as spikes) across involved frequency, since the frequency-dependent $\mathrm{RDR}_{\mathrm{mea}}$ is calibrated with global optimization across these frequencies. Sensitivity analysis was performed on eight calibration materials (similar to numerical assessment) with several measurement setups, where only S_1 sensitivity plots of two setups were shown in Fig. 11 for conciseness. Setup I is identical to the setup in the numerical assessment, whereas Setup II is slightly modified to match the

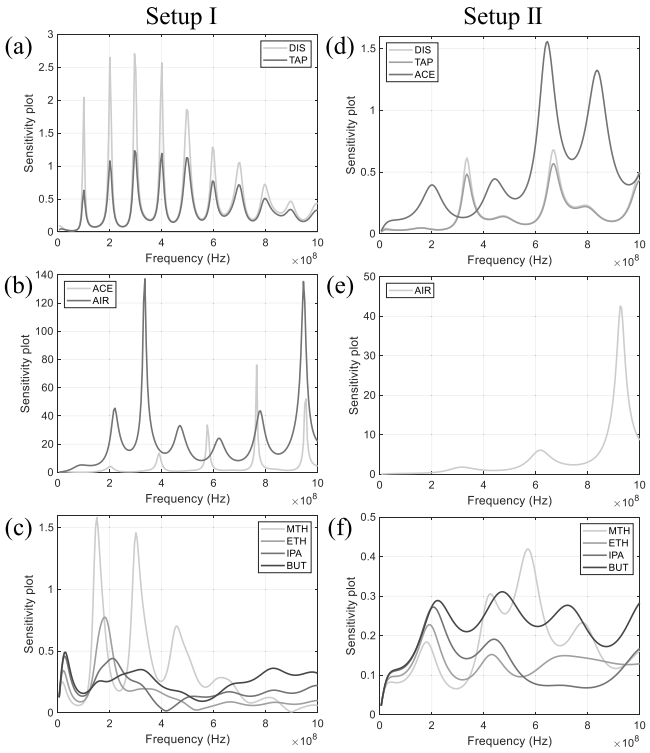

Fig. 11. Sensitivity plots for different calibration materials using (a)–(c) Setup I and (d)–(f) Setup II.

probe design in experimental acquisition later, which comprised of a 150-mm MS ($Z_p = 97\ \Omega$, $\varepsilon^*_{\mathrm{MS}} = 10$ with resulting $Z_{\mathrm{cMS}} = 30.7\ \Omega$) and a 50-mm SS with $Z_p = 97\ \Omega$. Sensitivity plots for Setups I and II are shown at two separate sides, with various materials presented in different subfigures according to their range. As observed in nondispersive materials for both setups, there are unfavorable sensitivity spikes with very high value contrast compared to their average sensitivity values. These high sensitivity difference across the frequency would affect the calibration accuracy and consistency, so these four nondispersive materials are deemed unsuitable as calibration materials. On the other hand, most dispersive materials have evenly distributed values with no high contrast spikes, except for MTH in Setup I, which presents some unfavorable spikes with value contrast as high as three times the average value. Other three dispersive materials (e.g., ETH, IPA, and BUT) have evenly distributed sensitivity curves, deeming them to be appropriate as calibration materials. Their sensitivity curves were further verified in other measurement setups and demonstrated similar sensitivity distribution with no significant spikes (omitted for simplicity).

The calibration robustness of *GlobalSearch* algorithm was assessed, using IPA as the appropriate calibration material in Setup II. TDR signal was forward modeled for Setup II and was processed following the standard signal processing procedure to extract $\mathrm{RDR}_{\mathrm{mea}}$. The frequency range used in the system parameter calibration is from 1 MHz to 1 GHz. Calibration was performed on four system parameters, namely, L_{MS}, $\varepsilon^*_{\mathrm{MS}}$, L_{SS}, and Z_{pSS}, excluding Z_{cLC} and Z_{pMS} since they are codependent parameters with the first four. The supplied

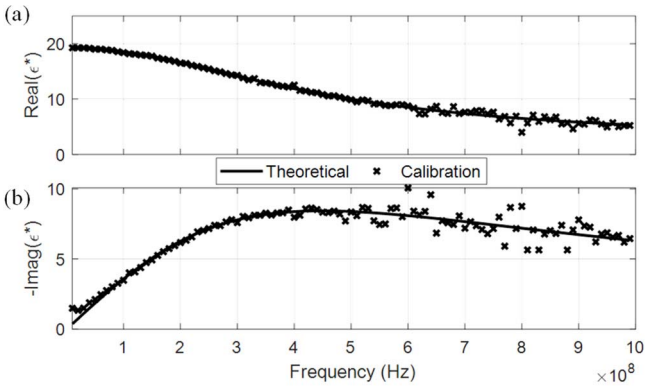

Fig. 12. Calibration result of Setup II using IPA as calibration material. (a) Real and (b) imaginary part of the estimated CDP spectrum of IPA.

initial guess in calibration for the four parameters was 0.5 m, 1, 0.30 m, and 10 Ω, respectively. System calibration was performed with *GlobalSearch* algorithm, and Setup II parameters L_{MS}, $\varepsilon^*_{\mathrm{MS}}$, L_{SS}, and Z_{pSS} were calibrated as 0.149952 m, 9.9759, 0.0502 m, and 97.97 Ω, correspondingly, which are very close to the forward-modeled parameters. The accuracy of the calibrated results was validated by plugging them back in the RDA analysis on simulated signals. Resultant CDP spectrums are shown in Fig. 12, where the estimated CDP spectrum using the calibrated parameters agrees well with theoretical values, where slight scattering of imaginary parts is observed at higher frequencies due to simulated noise.

RDA calibration is much more robust than the aforementioned SOL calibration, as the entire frequency range of a single-shot measurement is used to calibrate the four frequency independent system parameters (geometric factors and probe lengths) in RDA. Data redundancy from multiple frequencies in RDA calibration would mitigate potential measurement errors during calibration. Experimental evaluation on RDA is next demonstrated to assess its feasibility in field dielectric spectroscopy.

V. Experimental Evaluation

A. Measurement System and Probe Design

In order to evaluate RDA's feasibility under the influence of ambient noise in the real world, a measurement setup was established to acquire TDR signals for experimental evaluation, comprising of a broadband TDR device, a 1-m 50-Ω CFD-200 high-quality coaxial cable, and a modularized RDA probe. The broadband TDR pulser is TDR3000 device (Sympuls Aachen, Germany), which is the identical instrument used for acquiring input functions for numerical assessment. RDA probe was designed based on the aforementioned probe design considerations, which was tested with forward modeling and sensitivity analysis before fabrication. The probe designed for this preliminary study is named RDA-A1, consisting of a 100-mm 3-D printed composite dielectric block to serve as the dielectric insulator of MS, a200-mm stainless steel internal rod (external diameter of 5 mm), and a 250-mm stainless steel external casing with an internal diameter of 25 mm.

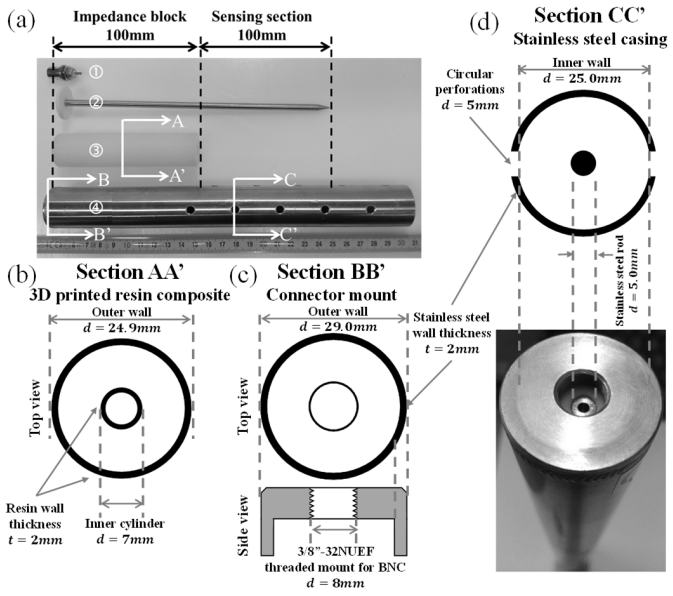

Fig. 13. Detailing of RDA-A1 coaxial probe. (a) Image of 3-D printed and lathed components. (b) AA' section of 3-D printed resin dielectric insulator. (c) BB' section of connector mount on top of external casing. (d) CC' section of perforated external casing.

Detailed probe configuration is shown in Fig. 13, where cross sections of the 3-D-printed dielectric insulator of MS, threaded connector mount on top of MS, and the external casing are shown in subplots Fig. 13(b)–(d), respectively.

Transition from LC to the internal stainless steel rod [extending from MS to SS, shown as component ② in Fig. 13(a)] is achieved by using a commercial MCI-7031 Bayonet Neil–Concelman (BNC) female bulkhead connector [component ① in Fig. 13(a)] and locked on top of the external casing [component ④ in Fig. 13(a)] using a threaded mount, as shown in Fig. 13(c). Dielectric insulator of MS is constructed from 3-D printed ultraviolet curing resin [component ③ in Fig. 13(a)], using a twin hollow cylinder configuration with 24.9 and 7.0 mm diameter. Both ends of the twin hollow cylinder are tightly sealed with 3-D printed caps. In order to increase the effective CDP within the MS and to reduce the required nominal MS length, filling material is injected with syringe into the dielectric insulator through two predrilled needle hole on top of the dielectric insulator. By injecting the filling material in one hole until it overflows through the other, the hollow space can then be fully filled without trapped air. Distilled water was opted as the filling material for the dielectric insulator as distilled water is nondispersive (within TDR target frequency range), nonconductive, and most importantly, easy to be obtained and safe to be handled. Wall thicknesses of the resin dielectric insulator and stainless steel casing are chosen uniformly as 2 mm for nominal mechanical strength. The stainless steel casing is perforated at equal intervals for SS region to allow MUT to flow freely into the coaxial cell. The tip of the internal rod [component ② in Fig. 13(a)] is sharpened to further minimize potential end fringing effect.

We need to determine six system parameters prior to RDA measurement, namely, $Z_{\mathrm{cLC}}, Z_{\mathrm{pMS}}, \varepsilon^*_{\mathrm{MS}}, L_{\mathrm{MS}}, Z_{\mathrm{pSS}}$, and L_{SS}.

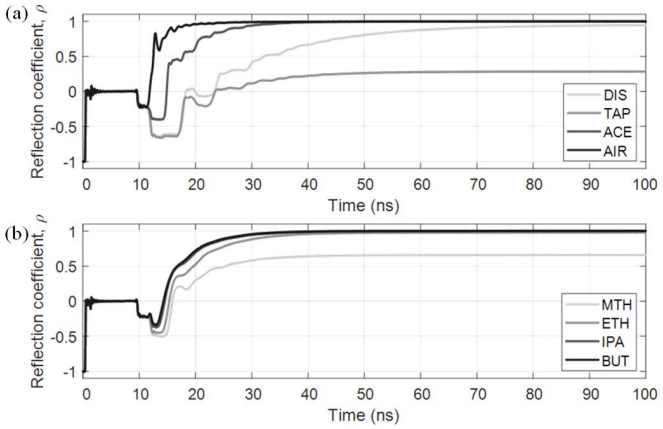

Fig. 14. Experimental TDR signals of RDA-A1 probe. (a) Less dispersive MUT. (b) Dispersive MUT.

Z_{cLC} is 50 Ω and the geometrical impedances (Z_p) of both MS and SS were designed as 96.5 Ω, where their internal and external conductors had identical dimension for single piece manufacturing. Both L_{MS} and L_{SS} were measured to be around 100 mm, whereas the effective $\varepsilon^*_{\mathrm{MS}}$ was uncertain as the MS was constructed using a 3-D printed hollow cylinder filled with distilled water. Fixing $Z_{\mathrm{cLC}} = 50\ \Omega$ and $Z_{\mathrm{pMS}} = 96.5\ \Omega$, $L_{\mathrm{MS}}, \varepsilon^*_{\mathrm{MS}}, L_{\mathrm{SS}}$, and Z_{pSS} were further calibrated in this study.

Eight MUTs were selected in the experimental evaluation, which are similar to those used in numerical assessment, covering material properties with different dielectric dispersions and electrical conductivities. Nondispersive MUTs were distilled water, tap water, acetone, and air, whereas the dispersive MUTs were MTH, ETH, IPA, and BUT. Their abbreviations are identical to those in Table I. TDR signals were measured using 5-ps sampling time under a controlled room temperature of 25 °C (± 0.2 °C), whereas the measured time window duration was 1×10^{-7} s. This data acquisition setup is capable of providing a measurement range from 1 MHz and 1 GHz with a frequency step of 5 MHz by zero-padding.

B. Performance Using RDA-A1 Probe

Measured experimental signals of all MUTs are displayed in Fig. 14, where subplot Fig. 14(a) and (b) shows the stacked time-domain signals of nondispersive and dispersive MUTs. Each TDR measurement was averaged from 12 signals to enhance the overall signal-to-noise ratio. The complete waveforms were recorded from the onset of step pulse. In practice, the data recording can start from several centimeters prior to the MS as the input signal is not required for RDA. There are no ambiguity in the window selection as the window selection was made unanimously at $t_1 = 7.5$ ns and $t_2 = 10.865$ ns for all MUTs in RDA-A1 setup. For presentation clarity, waveforms are properly scaled in Fig. 14 to have identical magnitude of step input. Notice that amplitude scaling is also not required for this source function independent RDA approach.

IPA was used to calibrate $L_{\mathrm{MS}}, \varepsilon^*_{\mathrm{MS}}, L_{\mathrm{SS}}$, and Z_{pSS}. Initial guesses of the system parameters supplied to the calibration

TABLE IV
CALIBRATION PARAMETERS FOR RDA-A1 PROBE

	L_{MS} $[m]$	ε^*_{MS}	L_{SS} $[m]$	Z_{pSS} $[\Omega]$
Direct measurement	0.10	10	0.10	96.5
Supplied initial guess	0.10	10	0.10	96.5
Calibrated parameters	0.104159	9.48944	0.101721	98.6712

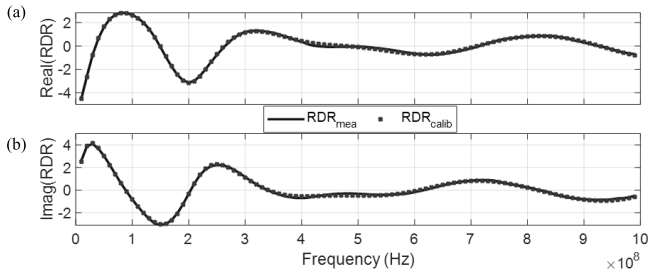

Fig. 15. Calibration results for RDA-A1 probe. (a) Real and (b) imaginary parts of calibrated RDR spectrum.

TABLE V
ABSOLUTE ERRORS OF EXPERIMENTAL DATA BETWEEN 1 MHz AND 1 GHz

MUT	Real CDP		Imaginary CDP	
	Mean	STD	Mean	STD
Distilled water	4.67	3.16	1.31	1.33
Tap water	2.70	3.32	2.60	3.80
Acetone	0.65	0.53	0.66	0.49
Air	0.17	0.21	0.20	0.15
Methanol	1.40	1.31	1.88	1.83
Ethanol	1.86	1.21	1.07	0.86
Isopropanol	0.45	0.31	0.46	0.28
Butanol	0.80	0.38	0.70	0.52

algorithm were estimated through direct measurement, as tabulated in Table IV. Z_{cLC} and Z_{pMS} were fixed as 50 and 96.5 Ω, respectively. Since RDA-A1 probe has a constant geometrical section for both MS and SS, we cross-checked and found that the values between the calibrated Z_{pSS}(98.6712 Ω) and the given Z_{pMS}(96.5 Ω) were reasonably close. It is noted that even if there were any error for the assumed Z_{pMS}, the induced error can be compensated by L_{MS} and $\varepsilon^*_{\text{MS}}$.

Based on the calibrated system parameters shown in Table IV, calibration results illustrating the fitting condition between $\text{RDR}_{\text{calib}}$ and RDR_{mea} are shown in Fig. 15. As the calibrated curve fits the measured curve closely, this implies that the system calibration was correct for all frequencies. Calibrated system parameters were supplied to subsequent CDP measurements of other MUTs.

CDP spectrums of all MUTs were measured following the standard RDA procedure. Figs. 16–19 show the measured CDP spectrums of the four nondispersive and the four dispersive MUTs. As an example, Fig. 16(c) and (d) further shows the data fitting condition for experimental data in distilled water. In all cases, the RDA inversion fits the data quite well. Similar to previous numerical assessment, quantitative analysis using absolute error of experimental data is shown in Table V.

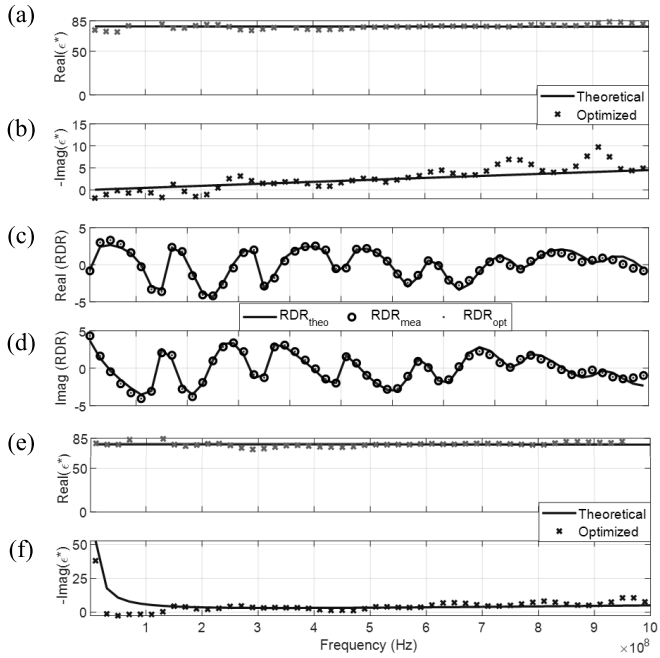

Fig. 16. RDA on experimental data. (a) Real CDP, (b) imaginary CDP, (c) real, and (d) imaginary parts of RDR spectrum for distilled water. (e) Real and (f) imaginary CDP of tap water.

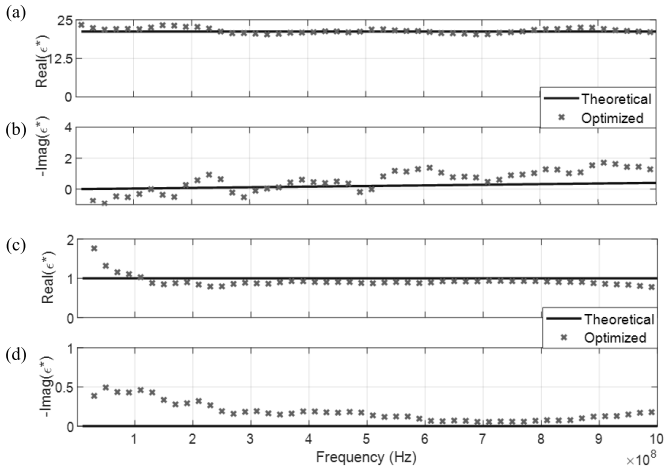

Fig. 17. RDA on experimental data. (a) Real and (b) imaginary CDP of acetone. (c) Real and (d) imaginary CDP of air.

IPA is first inspected in Fig. 19(a) and (b) since it was the calibration material for this experimental data. CDP spectrum measured for IPA matches the theoretical spectrum from 1 MHz to 1 GHz with very minor deviation in the imaginary part. This further confirmed that the calibration is effective. CDP spectrums for DIS and TAP are slightly scattered for certain frequencies, but their measured value fits the theoretical value quite well for a wide bandwidth. The electrical conductivity of TAP is around 300 μS/cm, and observing from the imaginary CDP fitting at lower frequencies in Fig. 16(f), electrical conductivity's contribution is also well captured. Although the absolute errors of both DIS and TAP

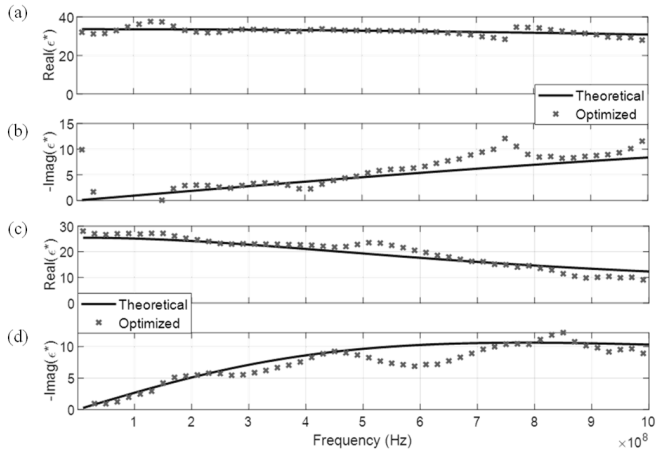

Fig. 18. RDA on experimental data. (a) Real and (b) imaginary CDP of MTH. (c) Real and (d) imaginary CDP of ETH.

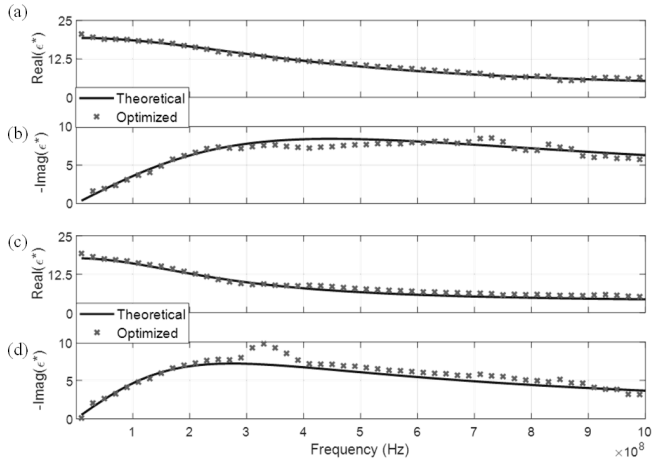

Fig. 19. RDA on experimental data. (a) Real and (b) imaginary CDP of IPA. (c) Real and (d) imaginary CDP of BUT.

are much larger than other MUTs, their percentage errors are still well within 6%. As for the nondispersive ACE, Fig. 17(a) and (b) shows some oscillation in the CDP spectrum near the theoretical value, but the mean deviation is still at an acceptable range of $0.65 + 0.66i$. This is attributable to a higher noise (reflection) at the LC-MS interface, probably due to less than ideal connection. Fig. 17(c) and (d) shows that the estimated CDP spectrum of AIR matched the theoretical values closely for all frequency. Effective frequency range of experimental data is slightly reduced to 20 MHz for AIR, probably due to higher ambient noise and some minor mismatches in the connectors. Experimental errors can be reduced by improving the connections at LC-MS and MS-SS interfaces. Nevertheless, it is remarkable for a probe with such short length to be capable of characterizing materials with such low dielectric permittivity, without the hassle of window picking in the time-domain signals.

CDP spectrums for dispersive signals are actually the main target for the development of this RDA approach. For DRA and MRA approach, signal leakage and truncation caused by dispersive signals are inevitable because r_1 in these two methods could not reach its steady state due to the length limitation of SS. Dispersive MUTs usually have signals with highly dispersed time-domain signals with increased rise time, causing signal leakage from r_1 into r_2 or $r_{\text{remaining}}$. Figs. 18 and 19 show the four alcohols (MTH, ETH, IPA, and BUT) measured in this study. Compared to experimental evaluation in MRA [44], the measured spectrums of all dispersive MUT in this study are significantly better in terms of absolute error and effective bandwidth, owing to minimal signal leakage and truncation. The mean absolute errors for dispersive type MUT are all below 1.86 for both real and imaginary parts of CDP. Closer inspection revealed that CDP spectrum of MTH and ETH is relatively scattered at high frequencies, potentially due to relatively lower sensitivity for that region. Nonetheless, this outcome has already improved over MRA as the measured values oscillated near their theoretical values. Measured CDP spectrums of IPA and BUT also match their theoretical curves very well across all frequencies from 1 MHz to 1 GHz.

VI. Conclusion

A novel self-referencing dielectric spectroscopy using one-shot measurement of TDR signal is proposed for characterizing CDP spectrum over a broad frequency range. The proposed RDA includes a nonconductive, nonresistive, and nondispersive MS between the leading section and the sensing section. This MS provides a reliable self-referencing signal by allowing the first major reflection signal to achieve its steady state, prior to the arrival of subsequent reflections from the sensing section. Measurement performance of RDA was validated with numerical and experimental validation on TDR signals of MUT with different dielectric properties. The mean absolute errors of all measured CDP spectrum within 1 MHz to 1 GHz were found lower than $0.9 + 0.8i$ and $4.7 + 2.6i$ in numerical and experimental assessment, respectively. Experimental errors can be reduced by improving the connections at LC-MS and MS-SS interfaces.

The novel features of RDA are.

1) It is inherently independent of the source function, instrument mismatch, and cable resistance.
2) One-time robust calibration of only four frequency-independent system parameters using a standard well-known material. No recurring calibration is required after certain period or change of TDR instrument.
3) It is a general framework without major restrictive assumptions and with all probe parameters explicitly expressed, giving great flexibility for probe design (e.g., geometric impedance, probe length, and end condition).

These features give users higher freedom in their system design to suit their measurement environment. In particular, RDA is feasible in long-term automated monitoring in natural or engineering environments, even without recurring system calibration. The fixed time window at the MS allows the usage of ultrashort probes to achieve high spatial resolution measurements.

Model-free point inversion at each single frequency was carried out in this study to show the robustness of RDA

method. Inversion regularization or model-based inversion by inverting the model parameters of known dielectric model can be implemented for further improvements. For measurement setups with inevitably high resistive loss, the total elimination of cable resistance effect from RDA is recommended to be further investigated to extend bandwidths at lower frequencies.

REFERENCES

[1] U. Kaatze, "Measuring the dielectric properties of materials. Ninety-year development from low-frequency techniques to broadband spectroscopy and high-frequency imaging," *Meas. Sci. Technol.*, vol. 24, no. 1, 2013, Art. no. 012005, doi: 10.1088/0957-0233/24/1/012005.

[2] K. S. Cole and R. H. Cole, "Dispersion and absorption in dielectrics I. Alternating current characteristics," *J. Chem. Phys.*, vol. 9, no. 4, p. 341, 1941, doi: 10.1063/1.1750906.

[3] J. C. Maxwell, "VIII. A dynamical theory of the electromagnetic field," *Philos. Trans. Roy. Soc. London*, vol. 155, pp. 459–512, Dec. 1865, doi: 10.1098/rstl.1865.0008.

[4] A. Lewandowski, A. Szypłowska, M. Kafarski, A. Wilczek, P. Barmuta, and W. Skierucha, "0.05–3 GHz VNA characterization of soil dielectric properties based on the multiline TRL calibration," *Meas. Sci. Technol.*, vol. 28, no. 2, Feb. 2017, Art. no. 024007, doi: 10.1088/1361-6501/28/2/024007.

[5] A. Szypłowska *et al.*, "Impact of soil salinity, texture and measurement frequency on the relations between soil moisture and 20 MHz-3 GHz dielectric permittivity spectrum for soils of medium texture," *J. Hydrol.*, vol. 579, Dec. 2019, Art. no. 124155, doi: 10.1016/j.jhydrol.2019.124155.

[6] S. D. Logsdon, "Soil dielectric spectra from vector network analyzer data," *Soil Sci. Soc. Amer. J.*, vol. 69, no. 4, pp. 983–989, 2005, doi: 10.2136/sssaj2004.0352.

[7] H. Fellner-Feldegg, "Measurement of dielectrics in the time domain," *J. Phys. Chem.*, vol. 73, no. 3, pp. 616–623, Mar. 1969, doi: 10.1021/j100723a023.

[8] A. M. Nicolson and G. F. Ross, "Measurement of the intrinsic properties of materials by time-domain techniques," *IEEE Trans. Instrum. Meas.*, vol. IM-19, no. 4, pp. 377–382, Nov. 1970, doi: 10.1109/TIM.1970.4313932.

[9] T. A. C. M. Claasen and M. J. C. van Gemert, "Approximate solutions in multiple reflection time domain spectroscopy," *J. Chem. Phys.*, vol. 63, no. 1, pp. 68–73, Jul. 1975, doi: 10.1063/1.431098.

[10] R. H. Cole, "Evaluation of dielectric behavior by time domain spectroscopy. I. Dielectric response by real time analysis," *J. Phys. Chem.*, vol. 79, no. 14, pp. 1459–1469, Jul. 1975, doi: 10.1021/j100581a022.

[11] Y. D. Feldman, Y. F. Zuev, E. A. Polygalov, and V. D. Fedotov, "Time domain dielectric spectroscopy. A new effective tool for physical chemistry investigation," *Colloid Polym. Sci.*, vol. 270, no. 8, pp. 768–780, Aug. 1992, doi: 10.1007/BF00776148.

[12] M. J. C. van Gemert, "Evaluation of dielectric permittivity and conductivity by time domain spectroscopy. Mathematical analysis of Fellner-Feldegg's thin cell method," *J. Chem. Phys.*, vol. 60, no. 10, pp. 3963–3974, May 1974, doi: 10.1063/1.1680844.

[13] A. H. Clark, P. A. Quickenden, and A. Suggett, "Multiple reflection time domain spectroscopy. Application to dielectric relaxation properties of aqueous systems in the time range to 10−10 to 10−4 s," *J. Chem. Soc., Faraday Trans. Mol. Chem. Phys.*, vol. 70, pp. 1847–1862, 1974, doi: 10.1039/F29747001847.

[14] H. Fellner-Feldegg, "Thin-sample method for the measurement of permeability, permittivity, and conductivity in the frequency and time domain," *J. Phys. Chem.*, vol. 76, no. 15, pp. 2116–2122, Jul. 1972, doi: 10.1021/j100659a010.

[15] K. Giese and R. Tiemann, "Determination of the complex permittivity from thin-sample time domain reflectometry improved analysis of the step response waveform," *Adv. Mol. Relaxation Process.*, vol. 7, no. 1, pp. 45–59, May 1975, doi: 10.1016/0001-8716(75)80013-7.

[16] M. J. C. van Gemert and A. Suggett, "Multiple reflection time domain spectroscopy. II. A lumped element approach leading to an analytical solution for the complex permittivity," *J. Chem. Phys.*, vol. 62, no. 7, pp. 2720–2726, Apr. 1975, doi: 10.1063/1.430857.

[17] R. H. Cole, "Evaluation of dielectric behavior by time domain spectroscopy. II. Complex permittivity," *J. Phys. Chem.*, vol. 79, no. 14, pp. 1469–1474, Jul. 1975, doi: 10.1021/j100581a023.

[18] R. H. Cole, S. Mashimo, and P. Winsor, "Evaluation of dielectric behavior by time domain spectroscopy. 3. Precision difference methods," *J. Phys. Chem.*, vol. 84, no. 7, pp. 786–793, Apr. 1980, doi: 10.1021/j100444a017.

[19] R. H. Cole, "Time domain reflectometry," *Annu. Rev. Phys. Chem.*, vol. 28, pp. 283–300, Oct. 1977, doi: 10.1146/annurev.pc.28.100177.001435.

[20] R. H. Cole, "Time-domain spectroscopy of dielectric materials," *IEEE Trans. Instrum. Meas.*, vol. IM-25, no. 4, pp. 371–375, Dec. 1976, doi: 10.1109/TIM.1976.6312244.

[21] R. H. Cole, "Bridge sampling methods for admittance measurements from 500 kHz to 5 GHz," *IEEE Trans. Instrum. Meas.*, vol. IM-32, no. 1, pp. 42–47, Mar. 1983, doi: 10.1109/TIM.1983.4315007.

[22] Y. Feldman *et al.*, "Time domain dielectric spectroscopy: An advanced measuring system," *Rev. Sci. Instrum.*, vol. 67, no. 9, pp. 3208–3216, 1996, doi: 10.1063/1.1147444.

[23] Y. D. Feldman, V. A. Goncharov, Y. F. Zuev, and V. M. Valitov, "Time domain treatment of TDS data for the lumped-capacitance method," *Chem. Phys. Lett.*, vol. 58, no. 2, pp. 304–306, Sep. 1978, doi: 10.1016/0009-2614(78)80300-5.

[24] Y. D. Feldman, V. A. Goncharov, Y. F. Zuev, and V. M. Valitov, "Treatment of TDS data for the lumped-capacitance method. Frequency-domain treatment," *Chem. Phys. Lett.*, vol. 65, no. 1, pp. 68–70, Aug. 1979, doi: 10.1016/0009-2614(79)80127-X.

[25] N. E. Hager, "Broadband time-domain-reflectometry dielectric spectroscopy using variable-time-scale sampling," *Rev. Sci. Instrum.*, vol. 65, no. 4, pp. 887–891, Apr. 1994, doi: 10.1063/1.1144917.

[26] S. C. Mehrotra, A. Kumbharkhane, and A. Chaudhari, "Theoretical and experimental aspects of time domain permittivity spectroscopy," in *Binary Polar Liquids*. Amsterdam, The Netherlands: Elsevier, 2017, pp. 1–43, doi: 10.1016/B978-0-12-813253-1.00001-X.

[27] R. H. Cole, J. G. Berberian, S. Mashimo, G. Chryssikos, A. Burns, and E. Tombari, "Time domain reflection methods for dielectric measurements to 10 GHz," *J. Appl. Phys.*, vol. 66, no. 2, pp. 793–802, Jul. 1989, doi: 10.1063/1.343499.

[28] J. G. Berberian, "Time domain reflectometry: Bilinear corrections and extending the range of analysis beyond the quarter and half wavelength conditions," *J. Mol. Liq.*, vol. 56, pp. 1–18, Jul. 1993, doi: 10.1016/0167-7322(93)80015-N.

[29] T. S. Clarkson, L. Glasser, R. W. Tuxworth, and G. Williams, "An appreciation of experimental factors in time-domain spectroscopy," *Adv. Mol. Relaxation Interact. Process.*, vol. 10, no. 3, pp. 173–202, Jul. 1977, doi: 10.1016/0378-4487(77)80048-4.

[30] N. E. Hager and R. C. Domszy, "Monitoring of cement hydration by broadband time-domain-reflectometry dielectric spectroscopy," *J. Appl. Phys.*, vol. 96, no. 9, p. 5117, 2004, doi: 10.1063/1.1797549.

[31] A. Bandla, N. Hager, and M.-R. Tofighi, "Ultra-broadband material spectroscopy from scattering parameters obtained from time domain measurements," *J. Franklin Inst.*, vol. 354, no. 18, pp. 8747–8757, Dec. 2017, doi: 10.1016/j.jfranklin.2016.10.046.

[32] P. Sivagurunathan, K. Dharmalingam, K. Ramachandran, B. P. Undre, P. W. Khirade, and S. C. Mehrotra, "Dielectric studies on binary mixtures of ester with alcohol using time domain reflectometry," *J. Mol. Liquids*, vol. 133, nos. 1–3, pp. 139–145, 2007, doi: 10.1016/j.molliq.2006.08.058.

[33] B. G. Lone, P. B. Undre, S. S. Patil, P. W. Khirade, and S. C. Mehrotra, "Dielectric study of methanol-ethanol mixtures using TDR method," *J. Mol. Liq.*, vol. 141, nos. 1–2, pp. 47–53, May 2008, doi: 10.1016/j.molliq.2008.03.001.

[34] A. Cataldo, L. Catarinucci, L. Tarricone, F. Attivissimo, and E. Piuzzi, "A combined TD-FD method for enhanced reflectometry measurements in liquid quality monitoring," *IEEE Trans. Instrum. Meas.*, vol. 58, no. 10, pp. 3534–3543, Oct. 2009, doi: 10.1109/TIM.2009.2018009.

[35] T. J. Heimovaara, "Frequency domain analysis of time domain reflectometry waveforms: 1. Measurement of the complex dielectric permittivity of soils," *Water Resour. Res.*, vol. 30, no. 2, pp. 189–199, Feb. 1994, doi: 10.1029/93WR02948.

[36] R. Friel and D. Or, "Frequency analysis of time-domain reflectometry (TDR) with application to dielectric spectroscopy of soil constituents," *Geophysics*, vol. 64, no. 3, pp. 707–718, May 1999, doi: 10.1190/1.1444580.

[37] J. A. Huisman, A. H. Weerts, T. J. Heimovaara, and W. Bouten, "Comparison of travel time analysis and inverse modeling for soil water content determination with time domain reflectometry," *Water Resour. Res.*, vol. 38, no. 6, pp. 13-1–13-8, Jun. 2002, doi: 10.1029/2001WR000259.

[38] J.-P. Laurent and P. Ferrari, "*In-situ* time domain spectroscopy in soils: Possibilities, problems and some solutions," in *Proc. 4th Int. Conf. Electromag*, Weimar, Germany, May 2001, pp. 351–358.

[39] K. Kupfer, E. Trinks, N. Wagner, and C. Hübner, "TDR measurements and simulations in high lossy bentonite materials," *Meas. Sci. Technol.*, vol. 18, no. 4, pp. 1118–1136, Apr. 2007, doi: 10.1088/0957-0233/18/4/021.

[40] T. Bore, H. Bhuyan, T. Bittner, V. Murgan, N. Wagner, and A. Scheuermann, "A large coaxial reflection cell for broadband dielectric characterization of coarse-grained materials," *Meas. Sci. Technol.*, vol. 29, no. 1, Jan. 2018, Art. no. 015602, doi: 10/gd8kdc.
[41] B. P. Kwok, S. O. Nelson, and E. Bahar, "Time-domain measurements for determination of dielectric properties of agricultural materials," *IEEE Trans. Instrum. Meas.*, vol. IM-28, no. 2, pp. 109–112, Jun. 1979, doi: 10.1109/TIM.1979.4314778.
[42] C.-P. Lin, Y. J. Ngui, and C.-H. Lin, "A novel TDR signal processing technique for measuring apparent dielectric spectrum," *Meas. Sci. Technol.*, vol. 28, no. 1, 2017, Art. no. 015501, doi: 10.1088/1361-6501/28/1/015501.
[43] Y. J. Ngui, C.-P. Lin, and T.-J. Wu, "Dielectric spectroscopy using dual reflection analysis of TDR signals," *Sensors*, vol. 19, no. 6, p. 1299, Mar. 2019, doi: 10.3390/s19061299.
[44] C.-P. Lin, Y. J. Ngui, and C.-H. Lin, "Multiple reflection analysis of TDR signal for complex dielectric spectroscopy," *IEEE Trans. Instrum. Meas.*, vol. 67, no. 11, pp. 2649–2661, Nov. 2018, doi: 10.1109/TIM.2018.2822404.
[45] W. Feng, C. P. Lin, R. J. Deschamps, and V. P. Drnevich, "Theoretical model of a multisection time domain reflectometry measurement system," *Water Resour. Res.*, vol. 35, no. 8, pp. 2321–2331, Aug. 1999, doi: 10.1029/1999WR900123.
[46] C.-P. Lin and S.-H. Tang, "Comprehensive wave propagation model to improve TDR interpretations for geotechnical applications," *Geotech. Test. J.*, vol. 30, no. 2, pp. 90–97, 2007, doi: 10.1520/GTJ100012.
[47] G. F. A. L'Hospital, *Analyse des Infiniment Petits, Pour l'Intelligence des Lignes Courbes*. Paris, France: De L'Imprimerie. M. DC. XCVI, 1696.
[48] J. A. Nelder and R. Mead, "A simplex method for function minimization," *Comput. J.*, vol. 7, no. 4, pp. 308–313, 1965, doi: 10.1093/comjnl/7.4.308.
[49] J. W. Cooley and J. W. Tukey, "An algorithm for the machine calculation of complex Fourier series," vol. 19, no. 90, pp. 297–301, 1965.
[50] J. W. Tukey, "An introduction to the calculations of numerical spectrum analysis," in *Spectral Analysis of Time Series*. New York, NY, USA: Wiley, 1967.
[51] *MATLAB 2018a*, Mathwork, Nativk, MA, USA, 2018.
[52] U. Zsolt, L. Lasdon, J. C. Plummer, F. Glover, J. Kelly, and R. Marti, "Scatter search and local NLP solvers: A multistart framework for global optimization," *INFORMS J. Comput.*, vol. 19, pp. 328–340, Aug. 2007, doi: 10.1287/ijoc.1060.0175.
[53] W. Skierucha and A. Wilczek, "A FDR sensor for measuring complex soil dielectric permittivity in the 10–500 MHz frequency range," *Sensors*, vol. 10, no. 4, pp. 3314–3329, Apr. 2010, doi: 10.3390/s100403314.
[54] J. B. Hasted, *Aqueous Dielectrics*. New York, NY, USA: Chapman & Hall, 1973.
[55] T. Sato and R. Buchner, "Dielectric relaxation spectroscopy of 2-propanol-water mixtures," *J. Chem. Phys.*, vol. 118, no. 10, pp. 4606–4613, 2003, doi: 10.1063/1.1543137.
[56] C.-P. Lin, "Frequency domain versus travel time analyses of TDR waveforms for soil moisture measurements," *Soil Sci. Soc. Amer. J.*, vol. 67, no. 3, pp. 720–729, 2003, doi: 10.2136/sssaj2003.0720.

Yin Jeh Ngui received the B.Eng. degree (Hons.) in civil engineering from The Hong Kong Polytechnic University, Hong Kong, in 2013, and the Ph.D. degree in civil engineering (with emphasis in geotechnical engineering) from the National Chiao Tung University, Hsinchu, Taiwan, in 2019.

He is currently a Post-Doctoral Researcher with the Disaster Prevention and Water Environment (DPWE) Research Center, National Yang Ming Chiao Tung University, Hsinchu. He has over seven years of professional experience in near-surface geophysical survey, real-time monitoring of slope displacement and suspended sediment transportation, dielectric spectroscopy, and in-house hardware/software interfacing.

Dr. Ngui was a recipient of the Geotechnical Engineering Doctoral Thesis Award in 2019 from the Taiwan Geotechnical Society and three Best Student Paper Awards in 2013 for his undergraduate final year project from the Chartered Institution of Highways and Transportation, ASCE Hong Kong Section, and the Institute of Civil Engineers Hong Kong Association.

Chih-Ping Lin received the M.Sc. degree in civil engineering, the M.Sc. degree in electrical and computer engineering, and the Ph.D. degree from Purdue University, West Lafayette, IN, USA, in 1996, 1998, and 1999, respectively.

Since 1999, he has been a Faculty Member with the National Yang Ming Chiao Tung University, Hsinchu, Taiwan, where he is currently the Dean of the College of Engineering, the Director of Disaster Prevention and Water Environment (DPWE) Research Center, and a Distinguished Professor of the Department of Civil Engineering. His research interests include engineering monitoring based on electromagnetic time-domain reflectometry (TDR) and developments and applications of near-surface geophysics for solving engineering problems. The TDR-based measurements being developed range from soil moisture, suspended sediment concentration, water level, extensometer, localized shear deformation, scouring, and to dielectric spectroscopy.

Dr. Lin is a member of the International Society for Soil Mechanics and Geotechnical Engineering (ISSMGE), Environmental and Engineering Geophysics (EEGS), and Society of Exploration Geophysicists (SEG). He was a recipient of the ASTM Hogentogler Award in 2008. He served on the Board of the Environmental and Engineering Geophysical Society from 2010 to 2013 and is currently the Global Vice Chair of Near-Surface Geophysics Technical Section of SEG.